Contents

FOREWORD

This year's annual report actually covers the period of two years, since 2002 , for my coworkers and me, was a year with many acitivities aside from science. In September 2002, Mannheim hosted the European workshop of the Technical Group on Information optics (IOG 2002). At the same time, the 7th German Workshop, Optics in Computing Technology (ORT 2002) was hosted by us. I am very grateful to Sabine Volk, my secretary, who coordinated the planning and contributed a lot of work, to make these meetings possible. Mrs. Maria Kufner has joined us as assistant professor in the spring of 2002 and left us again in the autumn of the same year. I am very happy, that my former assistant, Jochen Bähr has founded a company, SMOS GmbH, commercializing micro-optical components fabricated by ion-exchange in glass. My two year term of the director of the institute for Computer engineering (Technische Informatik) also fell in this period. Changes in the university laws in Germany have effected, that the position of assistant does not exist any more – a change that may pose many problems for experimentally oriented chairs.

In 2003, the scientific output has again reached the standard level. The contributions by my Ph.D. student, Xiyuan Liu treat many aspects of the Ambiguity function. The contributions by Jochen Bähr, who is still partly involved in supervising student research, demonstrate the capabilities of ion-exchange. My Ph.D. student Slawomir Ziolkowski has devoted a large effort in the investigation of optical storage and my own contributions are mostly centered around the design of optical beam shaping elements. For all these works, we appreciate the enthusiastic and qualified support by Wolfgang Stumpfs, the technician at our chair.

Karl-Heinz Brenner

Members of the chair of Optoelectronics

1	**Prof. Dr. Brenner**	**Karl-Heinz**	27 00	brenner@uni-mannheim.de
2	**Dr. Bähr**	**Jochen**	26 92	jb@oe.ti.uni-mannheim.de
3	**Bootz**	**Felix**	26 94	ich@felixbootz.de
4	**Dietrich**	**Dennis**	26 97	dennis.dietrich@oe.ti.uni-mannheim.de
5	**Ehrbächer**	**Ulrich**	26 93	uehrbaec@oe.ti.uni-mannheim.de
6	**Holzer**	**Johannes**	26 97	jholzer@rumms.uni-mannheim.de
7	**Lang**	**Matthias**	26 97	malang@rumms.uni-mannheim.de
8	**Lehmann**	**Lars**	26 97	llehmann@rumms.uni-mannheim.de
9	**Lippet**	**Hannes**	26 98	hannes@lippet.de
10	**Liu**	**Xiyuan**	26 93	xiyuanl@rumms.uni-mannheim.de
11	**Ringelstein**	**Jan**	26 94	jringels@rumms.uni-mannheim.de
12	**Stumpfs**	**Wolfgang**	27 02	wstumpfs@oe.ti.uni-mannheim.de
13	**Trauter**	**Bastian**	26 97	btrauter@rumms.uni-mannheim.de
14	**Volk**	**Sabine**	27 04	office@oe.ti.uni-mannheim.de
15	**Wohlfeld**	**Denis**	26 98	wohlfeld@gmx.de
16	**Ziolkowski**	**Slawomir**	27 01	ziola@oe.ti.uni-mannheim.de

Non-paraxial wave propagation in absorbing materials

X. Liu, K.-H. Brenner

In order to compute the intensity distribution in absorbing materials, we have developed an extension of the non-paraxial Rayleigh-Sommerfeld description in the Fourier domain. To include absorption, we add an exponentially decaying term to the propagation factor.

1. Rayleigh-Sommerfeld form of propagation

The Rayleigh-Sommerfeld diffraction equation for propagation in dispersive media over a distance *z* can be expressed as

$$u_z(\vec{r}_\perp) = \iint \tilde{u}_0(\vec{k}_\perp)\, e^{i\vec{k}_\perp \cdot \vec{r}_\perp}\, e^{iz\sqrt{(nk_0)^2 - k_\perp^2}}\, \frac{d^2k_\perp}{(2p)^2} \qquad (1)$$

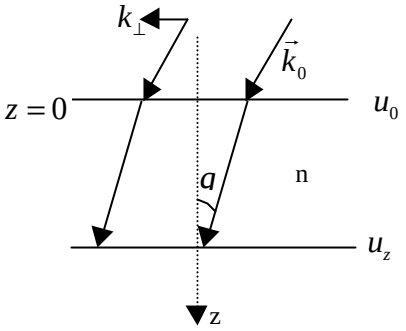

Here $\tilde{u}_0$ is the Fourier transform of the complex field u_0 at $z = 0$.

2. Absorption and complex index of refraction

For a plane wave, absorption along a distance *r* is expressed by

$$|u(r)| = |u_0| e^{-a r} \qquad (2)$$

with a as the absorption constant. For media, which absorb as well as refract, a complex index of refraction can be defined:

$$\hat{n} = n + i\,k \quad \text{with} \quad a = k\,k_0 = k\,\frac{w}{c} \qquad (3)$$

3. Rayleigh-Sommerfeld propagation in absorbing materials

Because absorption does not change the phase distribution in the material, we include the amplitude term $e^{-a|r|}$, which is introduced in the Rayleigh-Sommerfeld form of propagation by

$$e^{-a|r|} = e^{-a\frac{z}{\cos(q)}} = e^{-az\frac{nk_0}{\sqrt{(nk_0)^2 - k_\perp^2}}} \qquad (4)$$

Thus, the complete equation for propagation in absorbing materials can be written as

$$u_z(x,y) = \iint \tilde{u}_0(n,m)\, e^{i2p(xn+ym)}\, e^{iz\frac{2pn}{l}\sqrt{1-\frac{(n^2+m^2)l^2}{n^2}}}\, e^{-a\frac{z}{\sqrt{1-\frac{(n^2+m^2)l^2}{n^2}}}}\, dn\,dm \qquad (5)$$

Note, that the phase is proportional to the cosine of the angle, whereas the decay term is proportional to the invers cosine of the angle, which indicates that a simple extension of the refractive index into the complex would not be the appropriate solution.

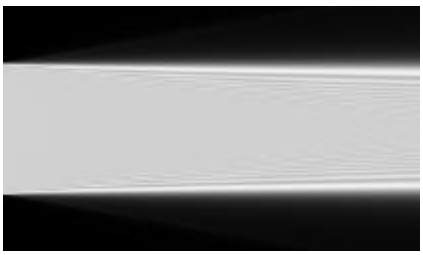

Fig.1: *Light amplitude in nonabsorbing material behind an aperture (a =0)*

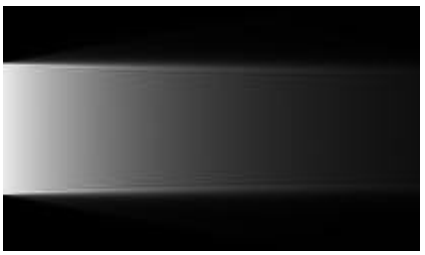

Fig.2: *Light amplitude in absorbing material behind an aperture (a =0.00008)*

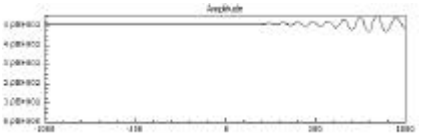

Fig.3: *Line scan from fig.1 for y=0*

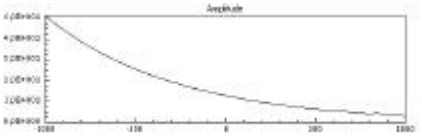

Fig.4: *Line scan from fig.2 for y=0*

Two discrete versions of the Ambiguity function of one-dimensional signals

X. Liu, K.-H. Brenner

The Ambiguity function (AF) has attracted considerable interest in recent years. This is due to the fact that the AF is a representation of signals in time and frequency simultaneously. As the AF has a number of interesting properties for signal analysis, it would be useful to have a discrete equivalent. We have investigated two definitions of the AF, which are discrete in time and also in frequency.

1. The symmetric version

The AF is defined by the integral:

$$A(x',n';u(x)) = \int u(x+\frac{x'}{2})\, u^*(x-\frac{x'}{2}) e^{-2\pi i x n'} dx = \int \tilde{u}(n+\frac{n'}{2})\, u^*(n-\frac{n'}{2})\, e^{2\pi i x' n} dn \tag{1}$$

For a signal u_k, which is periodic ($P = N \cdot d$) and discrete ($dx = d$), the discrete Fourier transform $\tilde{u}_l$ is defined by the equations

$$u_k = \sum_{l=0}^{N-1} \tilde{u}_l e^{2\pi i \frac{kl}{N}} \qquad\qquad \tilde{u}_l = \sum_{k=0}^{N-1} u_k e^{-2\pi i \frac{kl}{N}} \tag{2}$$

By combining eq. 1 with eq. 2, we obtain the symmetric definition of the discrete AF, with $u_{k+\bar{k}}\, u^*_{k-\bar{k}}$ showing symmetry in the index.

$$\begin{aligned} A(x',n';u(x)) &= \sum_{\bar{k}=0}^{N-1}\sum_{\bar{l}=0}^{N-1} A_{2\bar{k},\bar{l};u}\ \delta(x'-2\bar{k}d)\ \delta(n'-\frac{\bar{l}}{Nd}) \\ A_{2\bar{k},\bar{l};u} &= \sum_{k=0}^{N-1} u_{k+\bar{k}}\, u^*_{k-\bar{k}}\, e^{-2\pi i \frac{k\bar{l}}{N}} \end{aligned} \tag{3}$$

Because of the factor $1/2$ of x' in eq. 1, the AF has a spatial period of $2P = 2N \cdot d$ and a sampling distance $2d$ in the x'-domain. The disadvantage of this definition is that we can reconstruct only *N/2* values of u_k from the AF:

$$u_{k+\bar{k}}\, u^*_{k-\bar{k}} = \sum_{\bar{l}=0}^{N-1} A_{2\bar{k},\bar{l};u}\, e^{2\pi i \frac{k\bar{l}}{N}} \Rightarrow \quad u_{2\bar{k}} = \frac{\sum_{\bar{l}=0}^{N-1} A_{2\bar{k},\bar{l};u}\, e^{2\pi i \frac{\bar{k}\bar{l}}{N}}}{u^*_0} \qquad \bar{k} \le \frac{N}{2} - 1 \tag{4}$$

2. The asymmetric version

In analogy to the discrete definition of the Wigner function [1], we introduce an asymmetric version of the discrete AF, which results from an asymmetric equivalent of the AF, defined by

$$\begin{aligned} A(x',n';u(x)) &= \int u(x+\frac{x'}{2})\, u^*(x-\frac{x'}{2})\, e^{-2\pi i x n'} dx \qquad x_{new} = x_{old} + \frac{x'}{2} \\ &= \int u(x)\, u^*(x-x')\, e^{-2\pi i x n'} dx\, e^{\pi i x' n'} \end{aligned} \tag{5}$$

Combining eq. 5 with eq. 2, we obtain the asymmetric definition of the discrete AF, with $u_k\, u^*_{k-\bar{k}}$ having asymmetric indices.

$$\begin{aligned} A(x',n';u(x)) &= \sum_{\bar{k}=0}^{N-1}\sum_{\bar{l}=0}^{N-1} A_{\bar{k},\bar{l};u}\ \delta(x'-\bar{k}d)\ \delta(n'-\frac{\bar{l}}{Nd}) \\ A_{\bar{k},\bar{l};u} &= \sum_{k=0}^{N-1} u_k\, \tilde{u}_{k-\bar{k}}\, e^{-2\pi \frac{k\bar{l}}{N}}\, e^{\pi \frac{\bar{k}\bar{l}}{N}} \end{aligned} \tag{6}$$

Now the discrete AF has also a period of P and a sampling distance of d in x'-domain. Therefore we can now reconstruct all *N* values of u_k from the AF:

$$u_k\, u^*_{k-\bar{k}} = \sum_{\bar{l}=0}^{N-1} A_{\bar{k},\bar{l};u}\, e^{2\pi i \frac{k\bar{l}}{N}} \Rightarrow u_{\bar{k}} = \frac{\sum_{\bar{l}=0}^{N-1} A_{\bar{k},\bar{l};u}\, e^{2\pi i \frac{k\bar{l}}{N}}\, e^{-\pi i \frac{\bar{k}\bar{l}}{N}}}{u^*_0} \tag{7}$$

References

[1] K.-H. Brenner: "A discrete version of the Wigner distribution function", in *Proceedings of the EUSIPCO-83*, H.W. Schüssler (editor), Elsevier Science Publishers B.V, 307 - 310, North-Holland (1983)

Reconstruction of two-dimensional complex amplitudes from intensity measurements

X. Liu, K.-H. Brenner

The amplitude and phase recovery of optical fields with tomographic methods employing Wigner- or Ambiguity functions (WDF/AF) has been demonstrated extensively for the case of one-dimensional functions. For two-dimensional (2D) light distributions, the associated WDF/AF is four-dimensional, posing several implementation problems. Recently, we introduced a new concept, which allows to reconstruct arbitrary two-dimensional distributions, using only one-dimensional (1D) measurements [1].

1. Theory of reconstruction for complex 1D-signals

The AF $A(x',n';u)$ of a complex 1D-function $u(x)$ is alternatively defined as

$$A(x',n';u) = \int u(x+\frac{x'}{2})\, u^*(x-\frac{x'}{2})\, e^{-2\pi i x n'}\, dx = \int \tilde{u}(n+\frac{n'}{2})\, \tilde{u}^*(n-\frac{n'}{2})\, e^{2\pi i x' n}\, dn \qquad (1)$$

with the Fourier transform (FT) of $u(x)$ denoted as $\tilde{u}(n)$. To reconstruct a complex signal $u(x)$ from the AF, two main properties of the AF are used. First, the line distribution $A(0,n';u)$ corresponds to the FT of the intensity distribution of $u(x)$. Furthermore, light propagation in the AF representation corresponds to a shear of the AF. We denote $u_0(x)$ as the complex amplitude distribution at $z = 0$. The propagation to $z \neq 0$ in the Fresnel-approximation can be expressed in terms of the AF of $u_z(x)$ and the AF of $u_0(x)$ by:

$$A(x',n';u_z) = A(x' - \lambda z n', n'; u_0) \qquad (2)$$

The intensity $|u_z(x)|^2$ is related to the AF by:

$$\int u_z(x)\, u_z^*(x)\, e^{-2\pi i x n'}\, dx = A(0,n';u_z) = A(-\lambda z n', n'; u_0)\,, \qquad (3)$$

indicating that the FT of the intensity at z is a line along $(x'=0, n'=0)$ in $A(x',n';u_0)$. In order to obtain the complete $A(x',n';u_0)$, we have to measure a set of $|u_z(x)|^2$ at different z. The complex amplitude $u_0(x)$ can finally be computed from $A(x',n';u_0)$ by

$$u_0(x') = \frac{\int A(x',n';u_0)\, e^{\pi i x' n'}\, dn'}{|u_0(0)|}\, e^{i\cdot\arg[u_0(0)]} \qquad (4)$$

Since only the complex amplitude distribution is of interest, a scaling of the absolute value and a constant phase shift are usually irrelevant. It is required, however, that $|u_0(0)|$ is nonzero!

Practically we can only measure $|u_z(x)|^2$ for locations $|z| < z_{max}$, corresponding to a partial angular section of the AF. For the measurement of the remaining section of $A(x',n';u_0)$ we can use another property of the AF:

$$A(-n', x'; u(x)) = A(x',n'; \tilde{u}(x)) \qquad (5)$$

stating, that the FT results in a 90° rotation for the AF, allowing to measure $|\tilde{u}_0(x)|^2$ instead of $|u_\infty(x)|^2$.

Computed results ***Reconstructed results***

The modulus of the AF of the phase-element

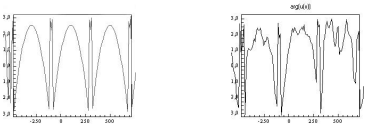

The phase of the phase-element

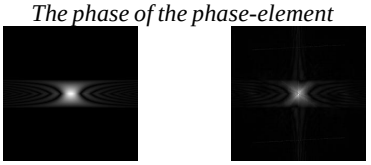

The modulus of the AF of the amplitude-element

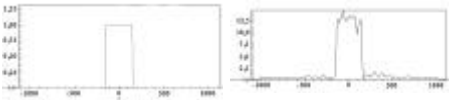

The modulus of the amplitude-element

2. Extension to the reconstruction of 2D-signals

Now we can describe, how the theory of reconstruction of 1D-signals can be used to reconstruct a 2D-signal. The reconstruction steps have to be repeated for a set of different, but fixed y-positions. By selecting a fixed y-position, say y_0, we are dealing with a 1D-complex amplitude $u_0(x)$. For the implementation, we require an optical setup, which performs 1D-transformations, i.e. a 1D-propagation operator and a 1D-Fourier & propagation operator. These optical operators are described in [2], performing 1D-operations, while the other dimension is considered as a series of parallel optical channels. In order to assess the performance of the new concept, we have selected a 2D-phase-element and a 2D-amplitude element. The experimental results, shown in the figures above, are in good agreement with the numerical simulation.

References

[1] X. Liu, K.-H. Brenner, "Reconstruction of two-dimensional complex amplitudes from intensity measurements", Optics Communications 225, p. 19 - 30, (2003)

[2] X. Liu, K.-H. Brenner, " One-dimensional optical operator for intensity measurement: Propagation operator and Fourier & propagation operator", this report, p. 7

One-dimensional optical operators for intensity measurement: Propagation operator and Fourier & propagation operator

X. Liu, K.-H. Brenner

Optical systems usually operate on two-dimensional (2D) distributions. Both, the wave propagation and the Fourier-transform operation realized by a lens perform a 2D transformation. Recently, we have encountered a situation, where we require one-dimensional (1D) wave propagation and Fourier-transformation, leaving the other dimension unchanged. Here we describe the experimental setups for a 1D propagation operator and a 1D Fourier & propagation operator.

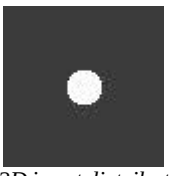

***Fig. 1**: 2D input distribution*

1. 1D propagation operator

In free space, a 2D light signal is propagated in 2D, shown in fig. 1 and fig. 2. A 1D-propagation operator, operating on the 2D-input distribution $u_0(x,y)$ must satisfy the relation

$$u_z(x,y) = \frac{1}{\sqrt{l\,z}} \exp(\frac{3p\,i}{4}) \exp(\frac{2p\,iz}{l}) \int u_0(x,y') \exp(\frac{ip}{l\,z}(y-y')^2)\, dy' \qquad (1).$$

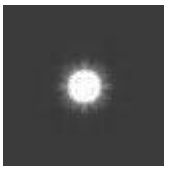

***Fig. 2**: 2D propagation result*

Fig. 3 demonstrates 1D-propagation of the input signal according to eq. 1. The setup in fig. 6 implements the desired 1D-propagation operator. In the reference plane at $z = 0$, the input $u_0(x,y)$ is located. In the detector plane, the output is obtained. To analyze the optical setup, we may observe the x- and y- axis separately. For the x-axis (fig. 7) it performs one-to-one imaging for every point at the input. The distance between the two lenses can be varied without any effect on the intensity distribution in the output plane. One advantage of this setup is that z_p can be positive and also negative, however z is bounded, $z > -(2f_y - f_x)$.

***Fig. 3**: vertical propagation*

2. 1D Fourier & propagation operator

An operator, which performs first a 1D-Fourier transform and then a 1D-propagation over a distance z_F, is shown in figures 9-11. For comparison, the 2D-Fourier transform result of the input signal (fig. 1) is shown in fig. 4. Fig. 5 demonstrates 1D-Fourier transformation of the input signal (vertical).

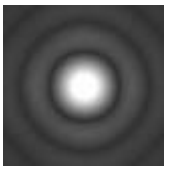

***Fig. 4:** 2D Fourier transform*

To analyze the optical setup, we again observe the x- and y- axis separately. For the x-axis (fig. 10) this system is identical to the 1D propagation operator. For the y-axis (fig.11) the system is basically a 2f-Fourier transformer. At $z = 2f_y$ we obtain $\tilde{u}(-\frac{x}{l\,f_y})$. The additional separation z_F allows us to combine the Fourier transform with a 1D-propagation operator. The distance z is bounded by $z > -(f_y - f_x)$.

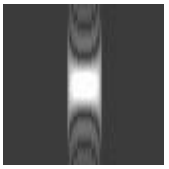

***Fig. 5:** vertical Fourier transform*

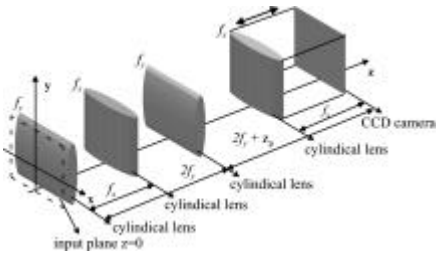

***Fig. 6**: 1D propagation operator for 2D input distribution*

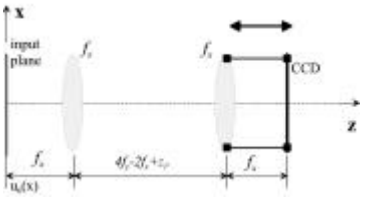

***Fig. 7:** x-view of the setup of the 1D propagation operator*

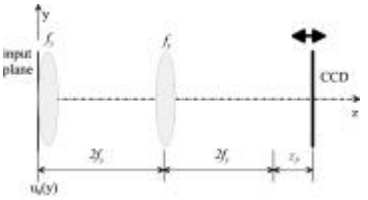

***Fig. 8**: y-view of the setup of the 1D propagation operator*

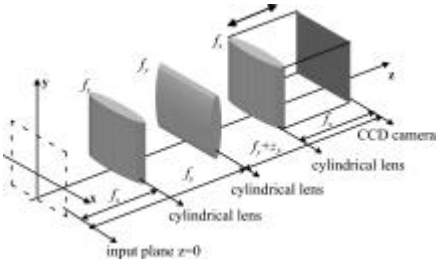

***Fig. 9**: 1D FT&propagation operator for 2D input distribution*

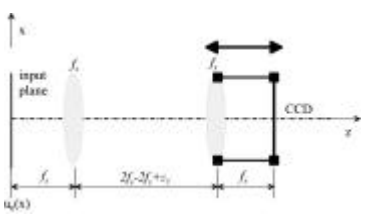

***Fig. 10**: x-view of the setup of the 1D FT&propagation operator*

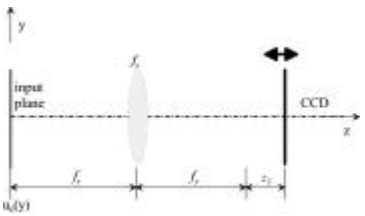

***Fig. 11**: y-view of the setup of the 1D FT&propagation operator*

MSI: different N.A. micro lenses on a common substrate

J. Bähr, SMOS GmbH

As demonstrated previously, the MSI technique (mask structured ion exchange) is a powerful tool for the realization of sophisticated designs of micro optical phase elements [1]. In our continuing work we realized diffraction limited micro lens arrays with high fill factor for several applications, such as for example Shack-Hartmann wavefront sonsors.

Here we report the realization of arrayed micro lenses with different focal power, side by side on the same substrate. The parameters of the lenses are: focal length: 2.6 mm (measured at HeNe), pitch of array 1: 173.0 micron, pitch of array 2: 130.0 micron, corresponding to Numerical Apertures of 0.025 and 0.033, each with Karthesian arrangement and 100% fill factor.

Both arrays were realized in a common fabrication process, with identical parameters i.e. temperature and concentration of the silver salt melt, duration of the exchange and post heating process. Thus the calculation of the mask structure of the two different arrays had to be performed on the same set of parameters. Figure 1 shows a subset of the sketch of the mask. The gap between the arrays is 500 microns. In figure 2 the intensity distribution in the focal plane is shown.

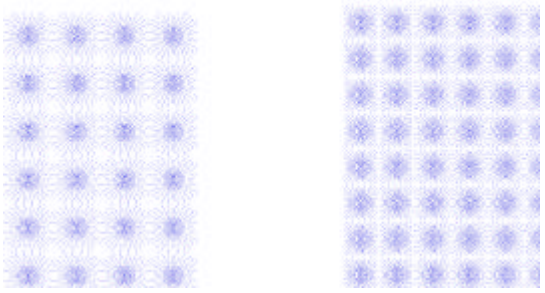

Fig. 1: *section of a sketch of the mask structure*

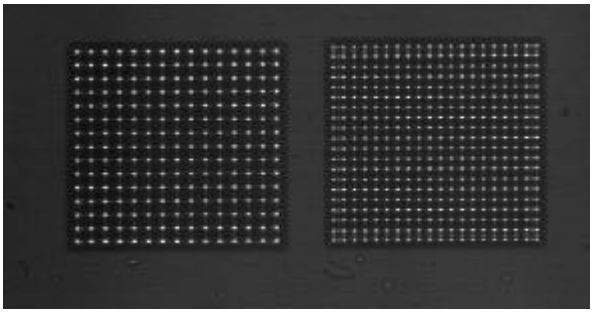

Fig. 2*: intensity distribution in the focal plane of the element*

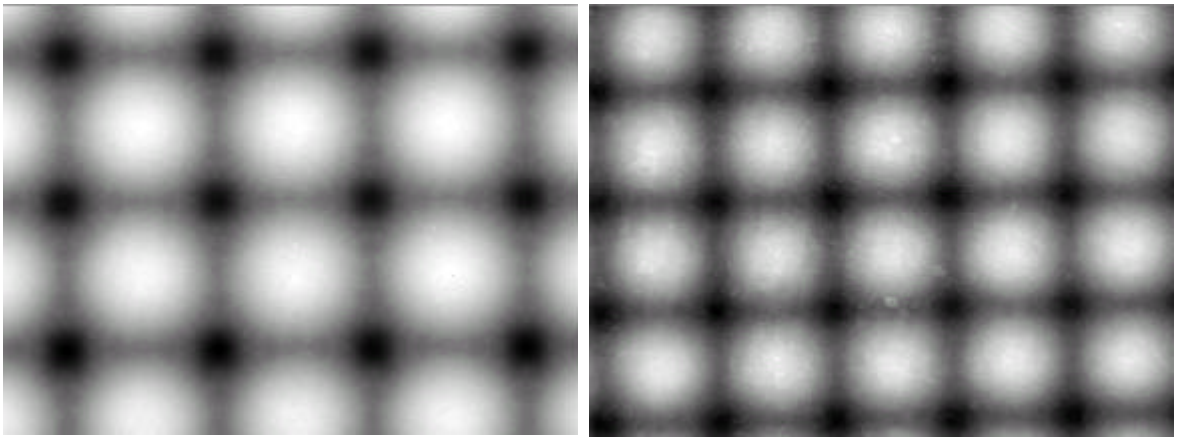

Fig. 3*: gray scale presentation of the phase distribution of array no. 1 (left) and array no. 2 (right) at equal magnification*

References

[1] J. Bähr, K.-H. Brenner, ”Realization of refractive continuous phase elements with high design freedom by mask structured ion exchange”, SPIE 46, annual meeting, Gradient Index, Miniature and Diffractive Optical Systems II, Proceedings of SPIE, Vol. 4437, p. 50-60, San Diego, (2001)

Numerical simulation of field-assisted ion exchange

D. Dietrich, J. Bähr

With field-assisted ion exchange it is possible to realise planar gradient index elements with deep phase profiles in a rapid exchange process, compared to purely thermal ion exchange. Therefore a glass substrate containing sodium is coated with a narrow titan layer, which is structured in an micro-lithographical process. This masked substrate is then brought into a silver salt melt and placed into an electric field. The silver ions in the melt diffuse through the mask apertures into the glass where they replace the sodium ions, which diffuse into the same direction, i. e. away from the masked side. The exchanged areas have different optical properties - mainly a higher refraction index - due to the silver-ion concentration.
The problem is to find a suitable mask pattern which results in the desired structure. This is a typical inverse problem, where the desired index distribution is given and the electric field resulting from the mask is to be found. Here we start with a mask pattern with some free parameters and we calculate the field induced ion migration.
The software "faSim" computes the shape of an exchanged structure based on a given mask pattern entered as a bitmap. Since effects caused by thermal ion exchange are negligible during the short process of field-assisted exchange, one can concentrate on the shape and position of the ion-front, i. e. the boundary between exchanged areas, populated with silver ions, and the areas where the sodium ions are still in their places. The movement of the ion-front is determined by the electric field through the mask apertures. To compute this field one computes the fields between every point $\vec{p}_i$ of the aperture and a virtual mirrored point $\vec{m}_i$ with opposite charge located at the position which results from mirroring $\vec{p}_i$ at the anode. The field-vector at the position $\vec{r}$ is determined by the Coulomb field:

$$\vec{E}(\vec{r}) = \frac{1}{4pe_0} \cdot \left(\sum_{i=0}^{n} \frac{q}{|\vec{r} - \vec{p}_i|^3} \cdot (\vec{r} - \vec{p}_i) + \sum_{i=0}^{n} \frac{-q}{|\vec{r} - \vec{m}_i|^3} \cdot (\vec{r} - \vec{m}_i) \right) \tag{1}$$

where q is the charge at the aperture and n is the number of aperture points
The silver ions and especially the ion front is affected by the electric field:

$$\vec{F}(\vec{r}) = q_{Ag^+} \cdot \vec{E}(\vec{r}) \tag{2}$$

where q_{Ag^+} is the charge of one silver ion.

For the i-th iteration step of the simulation the ion-front moves according to

$$\vec{r}_i = \vec{r}_{i-1} + \Delta t \cdot m \cdot \vec{F}(\vec{r}) \tag{3}$$

where m is the mobility of silver ions inside the glass media, $\vec{r}_i$ is the position of an ion-front point after the i-th iteration step and Δt is the time step during one iteration.
As an example we simulated an exchange process with the mask in Fig.1, which leads to an ion front depicted in Fig.2. An interferogram of an actual exchange result is shown in Fig.3.

Fig.1: *mask aperture*

Fig.2: *3D-plot of the ion-front surface*

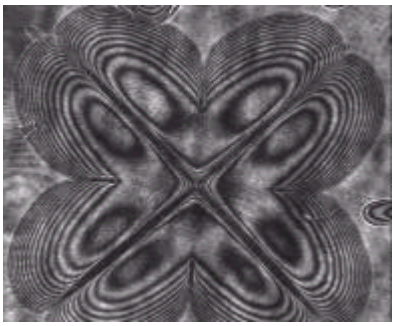

Fig.3: *interferogram of the experimental phase distribution*

References

[1] J. Bähr, „Analyse des feldunterstützten Silber-Natrium Ionenaustausches zur Herstellung planarer Mikrolinsen" (1996)
[2] J. Bähr, D. Dietrich, „Realization of a 4-Quadrant detector using field assisted ion exchange techniques", this report on page 10

Realization of a 4-Quadrant detector using field assisted ion exchange techniques

D. Dietrich, J. Bähr SMOS GmbH

For rapid wavefront analysis in astronomical applications (such as terrestrical telescopy) pyramidal sensors are suggested by several authors [1]. Such elements consist of four optical prisms, arranged in the shape of a pyramid, which is placed in the focus of a telescope. It can be considered as the two-dimensional extension of the Foucault-knife, suitable for detecting wave aberrations due to atmospheric turbulences. The baseline of the pyramid sensor is in the range of some hundreds of microns up to some millimeter. The beam deflection angle is in the range of a few degrees. For a sufficient splitting of the field, the rounding of the edges should be less than 10 microns.

A first prototype was realized using field assisted ion exchange in planar glass substrates [2]. In figure 1, a sketch of the mask for the exchange process is shown. It consists of four separated apertures. The silver ions migrate along the lines of the electrical current into the glass substrate. Since such paths do not overlap in principle (as depicted in fig. 2) four sharply separated sections of silver ion distributions are obtained. Figure 3 shows an interferogram of the distribution after an exchange of 20 minutes at 320°C and an applied electrical field of 270 V/mm. Figure 4 is a greyscale presentation of the inner region of the element. It demonstrates the sharpness of the edges. For further improvement of the single prisms (deviation of prism angle etc.) the shape of the mask apertures can be optimised, which is a part of a current diploma thesis.

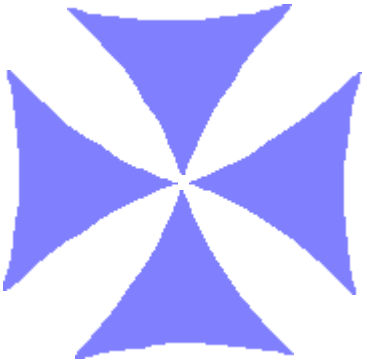

Fig. 1*: mask pattern used for the field assisted ion exchange process*

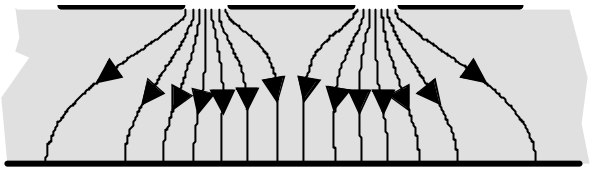

Fig. 2*: the shape of the electrical drift field is influenced by adjacent mask apertures*

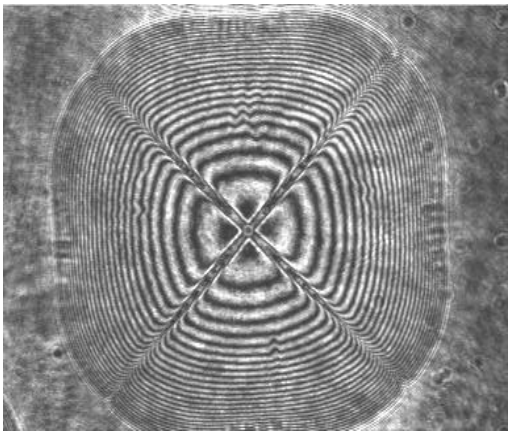

Fig. 3*: interferogram of the 4-quadrant element*

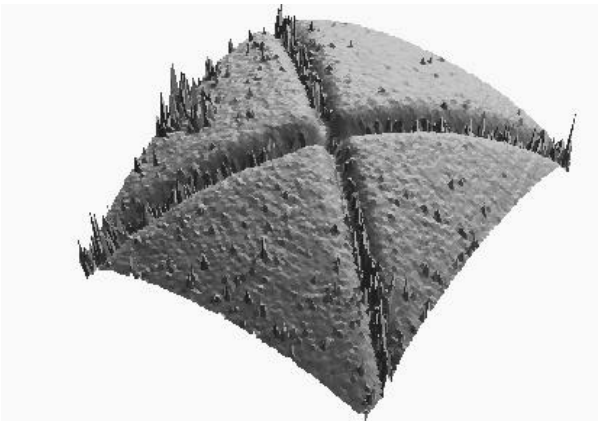

Fig. 4*: gray scale presentation of the central area of the 4-quadrant element depicted in fig. 3*

References

[1] S. Hippler et al.,"PYRAMIR: a near-infrared pyramid wavefront sensor for the Calar Alto adaptive optics system", SPIE 4839, p. 280, (2003)
[2] J. Bähr, K.-H. Brenner, "Realization and optimization of planar refracting microlenses by Ag-Na ion exchange techniques", Appl. Opt. 35, No. 25, 5102-5107, (1996)

Fabrication of continuous phase profiles in SU-8 resist

M. Kufner, D. Wohlfeld

The SU-8 resist is a well-known material for deep etch lithography. It enables structuring of some hundred micrometers of thick resist with moderate energies either by x-ray- or by UV-illumination [1]. By illumination with binary masks, aspect ratios of up to 100 were obtained with UV-illumination. With a modified lithographic process we have recently shown, that even continuous surface relief structures can be fabricated in SU-8 with structural heights as high as 500 µm.

Usually for the fabrication of binary structures, the resist is illuminated though a binary mask, determining laterally, where the resist will crosslink. In the longitudinal direction it is just necessary to assure that sufficient crosslinkage throughout the whole thickness of the resist layer is achieved, in order to make it insoluble. In contrast, here the aim is a spatial control of the crosslinkage, which affects also the longitudinal distribution [2].

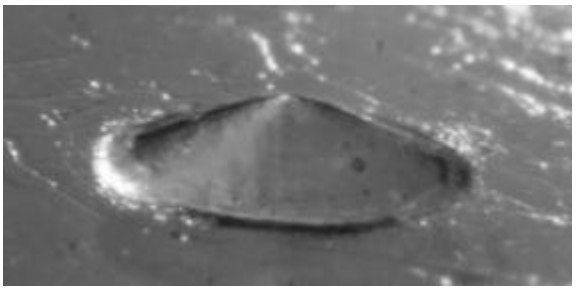

Fig. 1*: Conical structure with 2 mm diameter and 500 µm height*

In our experiments the SU-8 50 resist is coated on a substrate of float glass, which has been cleaned in H_2SO_4/H_2O_2 solution (3:1). The resist is smoothed on a hot plate for 10 min at 50°C and prebaked for 16h at 90°C. After irradiation and during development, the resist undergoes a special temperature cycle in order to prevent damages from stress in the thick resist layer.

For the fabrication of continuous surface structures we used grey scale masks to control the structural heights. The grey levels have been realized by dithered black and white patterns.
Examples of a conical and a pyramidal structure with 2 mm length or diameter respectively and heights of approximately 500 µm are shown in fig. 1 and 2. With this technique, almost arbitrary height distributions can be realised.

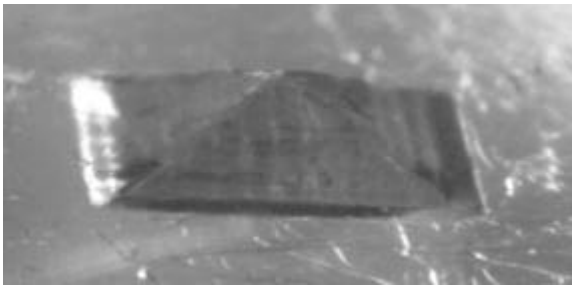

Fig. 2*: Pyramidal structure with 2 mm diameter and 500 µm height*

References:

[1] L. Singleton, M. Kufner, S. Megtert, “Consideration for the Deep X-ray Lithography with the SU-8 Resist”, Journal of Polymer Science and Technology 14 (2001) 4, p.649-656
[2] A. Rohrbach, K.-H. Brenner, “Surface-relief phase structures generated by light-initiated polymerization”, Applied Optics, Vol. 34, No. 22, p. 4747-4754, 1995

Characterisation of reflective surfaces by optical ray tracing

M. Lang, K.-H. Brenner

The most common measurement method for transparent or reflective optical surfaces is the interferometer. It is suitable for surfaces with height variations of a few tens of wavelengths. For larger height variations, 3D-measurement techniques can be used, if the surface has a certain degree of roughness. For transparent or reflective objects, there are not many methods available. To find an alternative method, we have investigated the reflection properties of structures with heights in the order of one millimeter and with a diameter of six millimeters.

The object is illuminated by a laser through a hole in a screen on which the reflected intensity can be observed. By mounting the object on two crosswise arranged step motors, the object can be scanned point by point. In the first tests, a known object was chosen. We have used a steel sphere with a defined radius because its height gradient is known and thus the reflected light distribution can be computed.

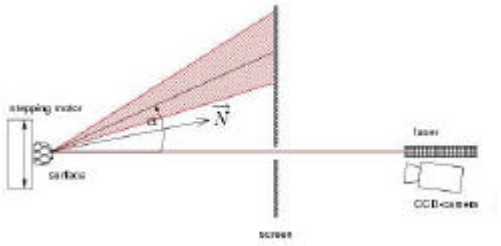

Fig. 1: *Assembly*

One of the major problems, that had to be solved, was that the beam diameter of about 0.5 mm leads to a significant beam widening. In a first approach, the reflection point in the center of the beam was computed as the center of gravity of the reflectance distribution, observed by a CCD camera.
As the camera stands off-axis, the geometry had to be corrected first. For this purpose the screen was equipped with six markers with known coordinates.
As the next step, the spatially corrected image in an xy-plane was transformed into the space of the unit vector s, i.e. the direction space. This corresponds to the situation, in which the reflection was observed on a hemispherical screen.
As shown in Fig. 2 the center of gravity of the distribution can be determined numerically. From this position, the gradient of the surface at the current position can be computed.

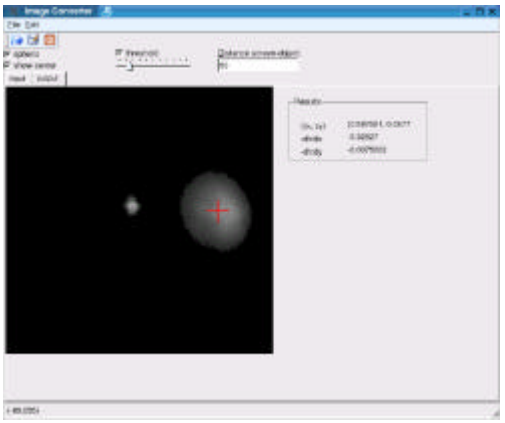

Fig. 2: *Evaluation software*

The result of a series of measurements is shown in Fig. 3. The computed surface gradient shows good symmetry, but there is a systematic deviation from the ideal curve, which is due a shift of the center of gravity at the edges of the sphere.
Fig. 4 shows a line scan and the corresponding image of a reflection distribution. From the line scan it is obvious that the right edge has a sharper decline than the left edge. The position of the center ray neither corresponds to the center of gravity nor to the maximum of the reflection distribution. Further research in this area will have to concentrate on techniques to correctly identify the center ray position.

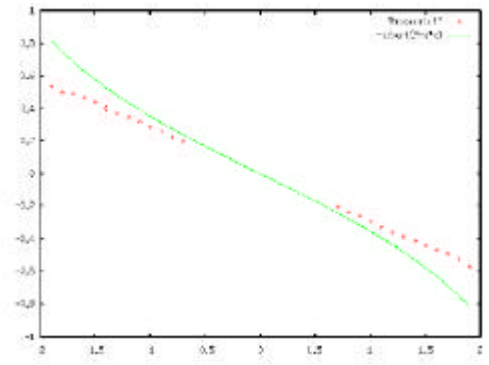

Fig. 3: *Plot of measurement results*

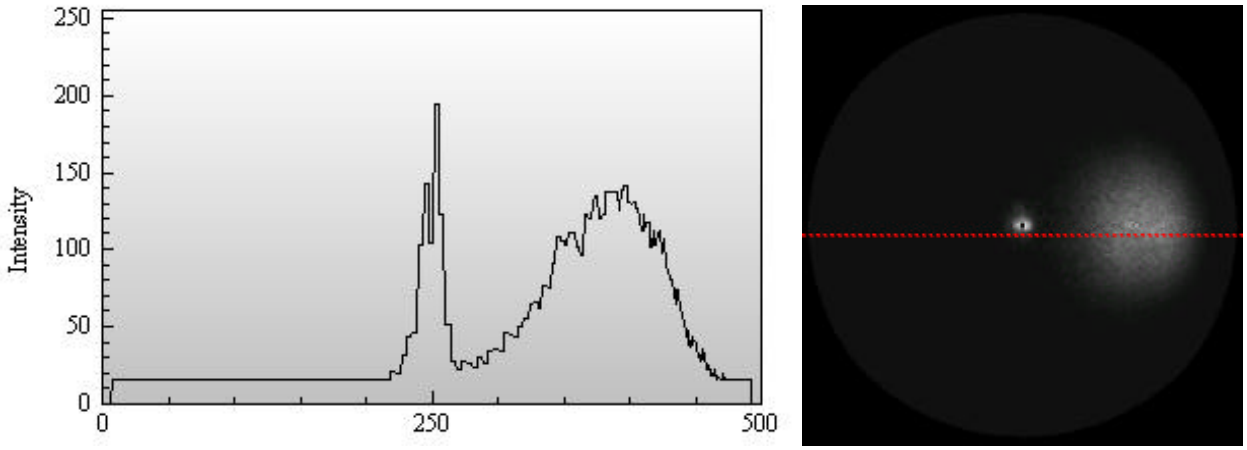

Fig. 4: *Line scan*

Vectorial treatment of focussing by a perfect lens using the Debye integral

S. Ziolkowski, K. –H. Brenner

In a previous work [1], we have determined the electric field distribution behind a perfect plano-convex focussing lens. The geometry of the system is represented in fig. 1. In these calculations, we have studied the electrical field distribution in the focal plane (E_3). Using the vectorial law of refraction (eq. 1), the propagation of a ray through the ideal focussing lens is described. By using Fresnel's equations, we can express the angle dependent electric field distribution behind the first surface (eq. 2) and the second surface of the lens (eq. 3).

$$\vec{t}_2 = \vec{t}_1 + \vec{N}\sqrt{n_2^2 - n_1^2 + \left(\vec{t}_1\vec{N}\right)^2} - \vec{t}_1\vec{N} \tag{1}$$

$$\vec{E}_1 = \left(\left(\vec{E}_0 \frac{\vec{t}_0 \times \vec{N}}{\left|\vec{t}_0 \times \vec{N}\right|}\right)\frac{2N_z}{N_z + \vec{t}_1\vec{N}}\right)\frac{\vec{t}_0 \times \vec{N}}{\left|\vec{t}_0 \times \vec{N}\right|} + \left(\left(\vec{E}_0 \frac{\vec{t}_0 \times \left(\vec{t}_0 \times \vec{N}\right)}{\left|\vec{t}_0 \times \left(\vec{t}_0 \times \vec{N}\right)\right|}\right)\frac{2N_z}{nN_z + \vec{t}_1\vec{N}/n}\right)\frac{\vec{t}_1 \times \left(\vec{t}_0 \times \vec{N}\right)}{\left|\vec{t}_1 \times \left(\vec{t}_0 \times \vec{N}\right)\right|} \tag{2}$$

$$\vec{E}_2 = \left(\left(\vec{E}_1 \frac{\vec{t}_1 \times \vec{e}_z}{\left|\vec{t}_1 \times \vec{e}_z\right|}\right)\frac{2t_{1z}}{t_{1z} + \vec{t}_{2z}}\right)\frac{\vec{t}_1 \times \vec{e}_z}{\left|\vec{t}_1 \times \vec{e}_z\right|} + \left(\left(\vec{E}_1 \frac{\vec{t}_1 \times \left(\vec{t}_1 \times \vec{e}_z\right)}{\left|\vec{t}_1 \times \left(\vec{t}_1 \times \vec{e}_z\right)\right|}\right)\frac{2t_{1z}}{t_{1z}/n + nt_{2z}}\right)\frac{\vec{t}_2 \times \left(\vec{t}_1 \times \vec{e}_z\right)}{\left|\vec{t}_2 \times \left(\vec{t}_1 \times \vec{e}_z\right)\right|} \tag{3}$$

By mapping the field distribution from a cartesian to a spherical coordinate system and using the Debye integral [2], we can compute the field distribution in and around the focal plane:

$$\vec{E}_3(x,y,z) = -\frac{ik_2}{2p}\iint_{\Omega}\frac{\vec{E}_2}{s_{2z}^2}\cdot\exp\left[ik_2 s_{2z} z\right]\cdot\exp\left[ik_2\left(s_{2x}x + s_{2y}y\right)\right]ds_{2x}ds_{2y} \tag{4}$$

Fig. 2 shows the intensity of the spot resulting from propagation of linear x-polarised light. The small images at the side show the intensity of the x-, y- and the z- field component. With these equations, the focal distribution for arbitrary input field distributions can be calculated.

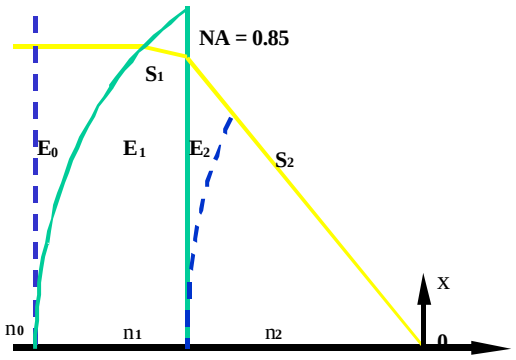

Fig.1: *Geometry of the optical system*

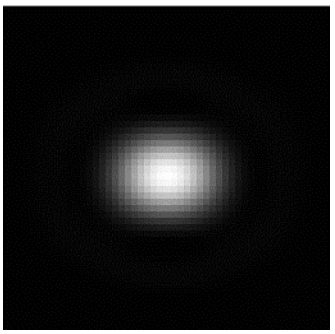

Fig. 2*: Focal intensity for linear x-polarised input*

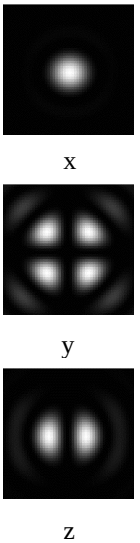

References

[1] K.–H. Brenner, “Polarisation analysis of an ideal plano-convex focusing lens”, Annual Report, Chair of Optoelectronics, University of Mannheim (2001)
[2] P. Török, P. Varga, Z. Laczik and G.R. Booker, J Opt. Soc. Am. A 12 (1995) 325

Influence of the polarisation state on the size of the focal spot

S. Ziolkowski, K. –H. Brenner

In the course of investigating the propagation of light through an optical system with a “perfect lens”, we have observed the influence of the polarisation state on the spot size. Unlike vectorial Debye-theory [1], we also included the refraction effects on the phase due to the lens.

In particular, we have studied two polarisation types: linear and circular polarisation. The circular polarisation is usually obtained from linear polarisation with a quarter-wave plate rotated at 45^0. This operation can by also represented by the equation:

$$E_{circ} = E_{x-pol} + i \cdot E_{y-pol} \tag{1}$$

Using a model for an ideal focussing lens, which we have developed earlier [2], we have simulated the propagation of polarised light through a lens using Frenel’s equations. To calculate the energy distribution in the focal spot, we used a Debye integral [2] which can be represented as:

$$\vec{E}_3(x,y,z) = -\frac{ik_2}{2p}\iint_{\Omega}\frac{\vec{E}_2}{s_{2z}^2}\cdot\exp\left[i\,k_2 s_{2z} z\right]\cdot\exp\left[ik_2\left(s_{2x}\,x + s_{2y}\,y\right)\right]ds_{2x}ds_{2y} \tag{2}$$

$\vec{E}_2$ is the electric field in a plane immediately behind the lens. The additional factor s_{2z} accounts for the transformation onto the unit sphere. The spot amplitude corresponding to different polarisation states is presented in fig. 1. It can be seen, that circular polarised light results in a rotational symmetry of spot, whereas linear polarisation results in an elliptic shape of the spot. The amplitude plot also indicates that the curve for circular polarisation lies between the curves for linear x- and y- polarisation. For an x-polarized wave-field, the y-extent roughly corresponds to the scalar case.

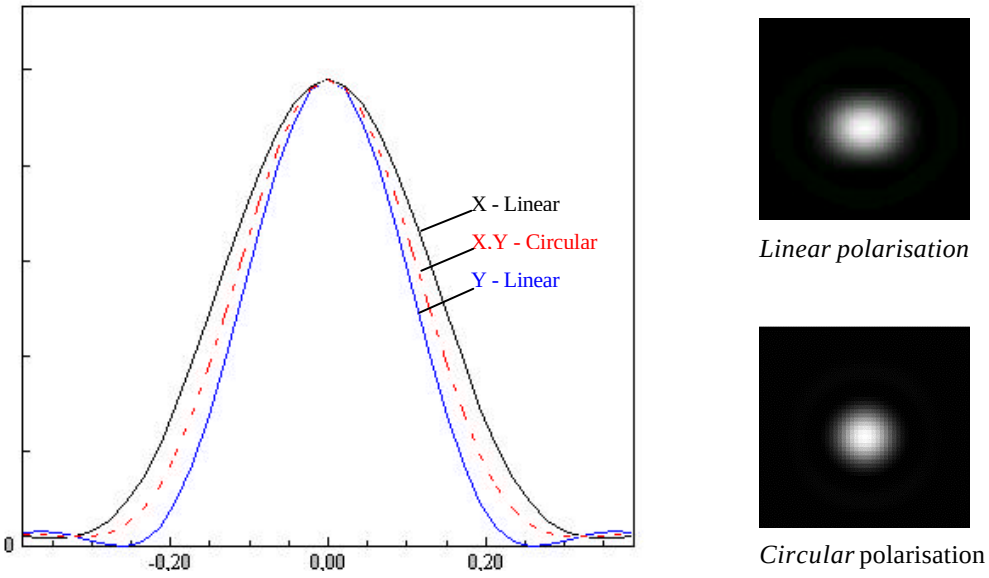

Fig.1: *spot intensity for different polarisation states (NA=0.85, l=405 nm)*

References

[1] P. Török, P. Varga, Z. Laczik and G.R. Booker, J Opt. Soc. Am. A 12 (1995) 325
[2] K.-H. Brenner, "Polarisation analysis of an ideal plano-convex focussing lens", annual report 2001, p. 14

Crosstalk reduction in optical storage using a phase element

S. Ziolkowski, K. –H. Brenner

Optical data storage systems use a focused beam of laser light to scan data tracks on rotating disk. The reflection of the focused spot is modulated as it passes over data marks. This modulation in the reflected beam is converted to a current signal by a detector. Large capacity storage disks require a high density of data tracks. Because of diffraction limits, in most of case, the spot diameter is wider than the spacing between tracks. As a result of this situation, there is an increase of crosstalk, represented by an increase of jitter in the detector signal. Reduction of the crosstalk by land-groove recording and by exit pupil filtering was proposed in other papers [3]. In this paper, we have investigated an approach to reduce cross talk by applying a phase plate in the pupil plane.

In situations with low numerical aperture (NA), the process of focussing of the light by a lens can be represented by a Fourier transformation of a circular pupil, resulting in a Bessel function for the amplitude distribution. From this, the spot size is determined by the NA and the wave length:

$$d = 1{,}22 \cdot \frac{l}{NA} \tag{1}$$

In high NA situations, polarization aspects must be included in the description [1] and non-paraxial light propagation using the Debye [2] approximation has to be used. For linearly polarized light, an asymmetry of the spot shape is observed, which could be used to reduce the crosstalk. More degrees of freedom, however, can be obtained by modelling the shape of focus by changing the phase of the incoming light in the pupil plane.

We modeled the complete spot detection process, including passage through an ideal lens, vectorial Debye-propagation, reflection from a simulated pit-structure of a DVD (or BD) disk and a final integration on a detector. In the plane of the focussing lens, we have added a phase element, which was computed using the iterative Fourier transform algorithm (IFTA).

We determined the crosstalk signal from the ratio of total energy which is reflected from a single track without neighbor pits and the total energy reflected from a track with two extra neighborhood “error” tracks. Using a convolution algorithm, we have accelerated the calculation procedure. After that, we have determined the position dependent crosstalk signal, shown in fig. 2. By adding an optimized phase mask, fig. 3 illustrates that the crosstalk can be reduced by a suitable phase mask.

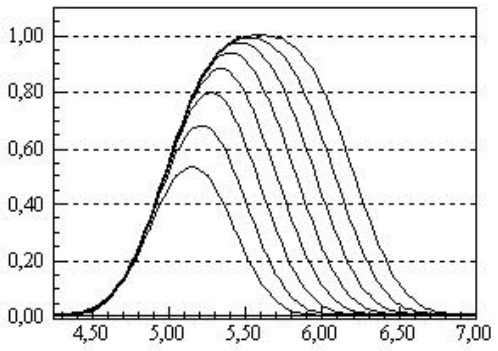

Fig. 1: *Detector response for 3T..10T symbols*

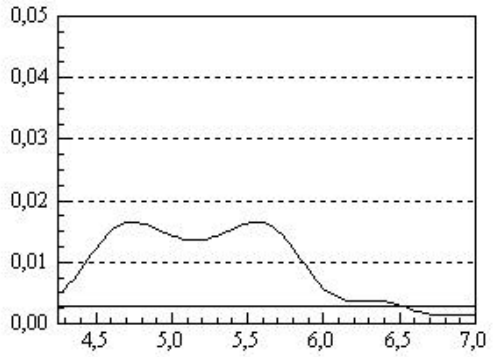

Fig. 2: *Crosstalk signal without phase element*

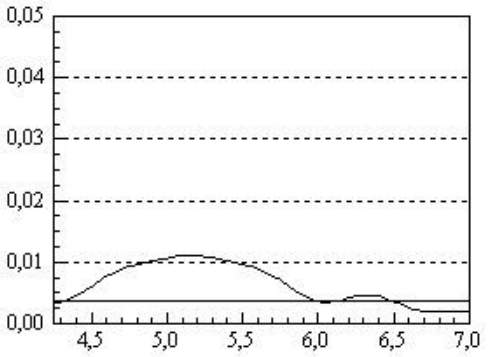

Fig. 3: *Crosstalk signal with phase element*

References

[1] K.–H. Brenner, “Polarisation analysis of an ideal plano-convex focusing lens”, Annual Report, Chair of Optoelectronics, University of Mannheim (2001)

[2] P. Török, “Annular focusing through a dielectric interface scanning and confining the intensity”, Pure Appl. Opt. 7, 1237-1248 (1998).

[3] S. Upton, “Fundamental principles of crosstalk in optical data storage”, Jpn. J. Appl. Phys. 38, 1608-1613 (1999).

Analysis of different interpolation methods for representing optical surfaces

S. Ziolkowski, K. –H. Brenner

The are many situations, where an optical surface is defined on a grid of height data with sampling distances dx, dy. In further calculations, such as ray tracing or in wave propagation methods, the height data are needed also between the sampling points. Consequently an interpolation scheme is needed, to compute the height for arbitrary x-y-positions. We can expect, that the quality of simulation, in this case, also depends on the choice of the interpolation method. As an extreme case, a piecewise linear interpolation scheme, used in many other applications, would not be appropriate for optical applications, where the surface gradient plays an important role. Here we report on the results of some of the most common interpolation approaches. Most interpolation schemes can be expressed as a convolution type operation:

$$u_n(x,y) = \sum_k \sum_l u(x_k, y_l) \cdot h(x - x_k) \cdot h(y - y_l) \tag{1}$$

$u(x_k, y_l)$ represents the samples of the height function u, and h is a suitable interpolation kernel.

a) Sinc interpolation
For band limited signals, the sinc-interpolation method is the most appropriate scheme, since it is derived from the sampling theorem and this case it offers a correct reconstruction of the source function. The interpolated function can be described by:

$$u_n(x,y) = \sum_{k,l} u(kdx, ldy)\,\mathrm{sinc}\left(\frac{x - k\cdot dx}{dx}\right)\mathrm{sinc}\left(\frac{y - l\cdot dy}{dy}\right) \tag{2}$$

where: $u(k\cdot dx, l\cdot dy)$ are the samples of the band limited source function, dx, dy are the sampling distances.

b) Biparametric interpolation
This is an interpolation method of second order. It can be represented for $|x| < dx, |y| < dy$ by:

$$\begin{aligned} u(x_k + x, y_l + y) = u_{k,l} &+ \frac{1}{2}\left(\left(u_{k-1,l} - u_{k+1,l}\right)\cdot\frac{x}{dx} + \left(u_{k,l-1} - u_{k,l+1}\right)\cdot\frac{y}{dy} \right) \\ &+ \frac{1}{2}\left(\left(u_{k-1,l} + u_{k+1,l} - 2\cdot u_{k,l}\right)\cdot\left(\frac{x}{dx}\right)^2 + \left(u_{k,l-1} + u_{k,l+1} - 2\cdot u_{k,l}\right)\cdot\left(\frac{y}{dy}\right)^2 \right) \end{aligned} \tag{3}$$

c) Bicubic interpolation
For the bicubic interpolation, we have used the interpolation kernel function *h(x)* defined by Keys [1].

We have applied these approaches to a phase element with an original size of 32x32, which was interpolated to a size of 256x256. It can be seen that the sinc-interpolation produces severe artifacts, in cases where the requirement of band limitation is not fulfilled completely. The biparametric interpolations operates significantly faster than the bicubic interpolation. The height reproduction of the two methods is comparably accurate, but the reproduction of the surface gradients is superior with bicubic interpolation for spherical surfaces.

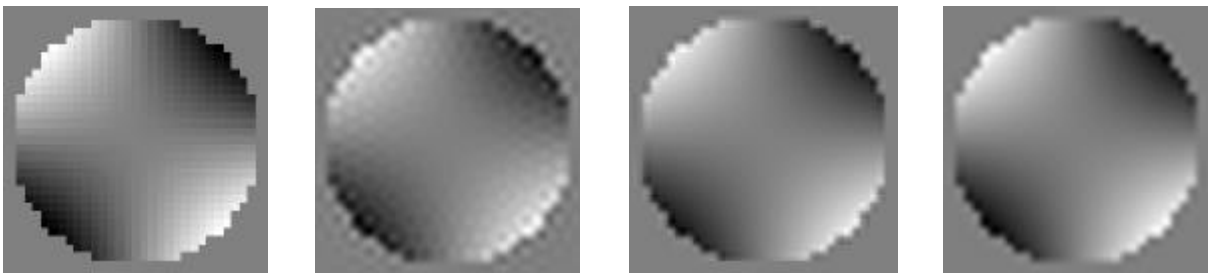

(a) (b) (c) (d)

Fig.1: *a) Source (32x32), b) Sinc interpolation, c) Biparametric interpolation, d) Bicubic interpolation*

References

[1] R. G. Keys, “Cubic convolution interpolation for digital image processing”, IEEE Trans. Acoust., Speach, Signal Processing, vol. ASSP-29, no. 6, pp. 1153-1160, 1981

Beam shapes with a soft flat-top

K.-H. Brenner

The transformation of a Gaussian laser intensity into a flattened beam profile by beam shaping is useful in many application areas such as in high power laser operations, where the Gaussian beam shape leads to an inefficient usage of the available laser power due to loss at the focusing lens. For illumination purposes, flattening the Gaussian beam profile is necessary in order to achieve a homogeneous illumination. In communication as well as in optical storage, a flattened intensity is necessary to achieve diffraction limited spot sizes for coupling into single-mode fibers or for the readout of optical pits on a disk. In a practical application, an ideal flat top is not most desirable, since it results to ringing effects, when diffraction at the edges is taken into account. Another drawback of a perfect flat-top profile is the very high demand on position accuracy. A recent investigation has shown e.g. that for micro-optical beam shapers with a diameter of 3 mm, positioned close to the semiconductor laser, the position tolerance can be as low as 2 microns. An increase in positioning tolerance can be achieved by deviating from the perfect flat-top profile. In recent years, several different softened flat-top profiles have been suggested. The super-Gaussian, as well as Gori's flattened beam have the advantage, that the beam shape can be adjusted continuously from Gaussian shape to the ideal flat-top using one control parameter. In a recent paper, Li [1] has summarised theses profiles and added two new ones. For comparing these profiles, he emphasises the requirement that analytic solutions should exist for light propagation.

For beam shaping problems, one can impose a different requirement, as we want to do in this report. In order to solve the rotationally symmetric beam shaping problem analytically, a soft flat-top profile has to satisfy two requirements: the existence of an analytic form of the integral and an analytic form of the inverse of the power. The law of power conservation requires that

$$P_0(r_0) = \int_0^{2p}\int_0^{r_0} I_0(r)\, r\, dr\, dj = \int_0^{2p}\int_0^{r_F} I_F(r)\, r\, dr\, dj = P_F(r_F)\,. \qquad (1)$$

For the total power within a ring of radius r, an analytical expression should exist. For the Gaussian intensity I_0 on the left side of the equation, such an analytic expression exists. The same should be true for the soft flat-top distribution I_F on the right side of the equation.
The next problem is to derive an equation, which relates the output radius r_F to the input radius r_0. To this end, the integrated intensity I_F, i.e. the power as a function of the output radius r_F must be invertable. To our knowledge, none of the distributions described in Li's paper satisfy these requirements. Thus only numerical methods can be employed to design beam shaping elements with soft flat-top profiles.

We have recently discovered a variant of the super-Lorenzian, which satisfies both requirements, stated before. The soft flat-top profile we have proposed, is

$$I_F(r;N) = \left(\frac{1}{1+r^N}\right)^{\frac{2}{N}+1} \qquad (2)$$

With this definition, the analytic solution of the right side integral of eq. 1 is

$$P_F(r_F) = \frac{1}{2}\left(\frac{r_F{}^N}{1+r_F{}^N}\right)^{\frac{2}{N}} \qquad (3)$$

Furthermore, it is clear that eq. 3 can readily be inverted to solve for P_F. Together with eq. 1, the mapping relation $r_F(r_0)$ can be determined consecutively. This is the basis for designing the optical element. With this new definition, thus the complete beam shaping problem can now be solved fully analytically.

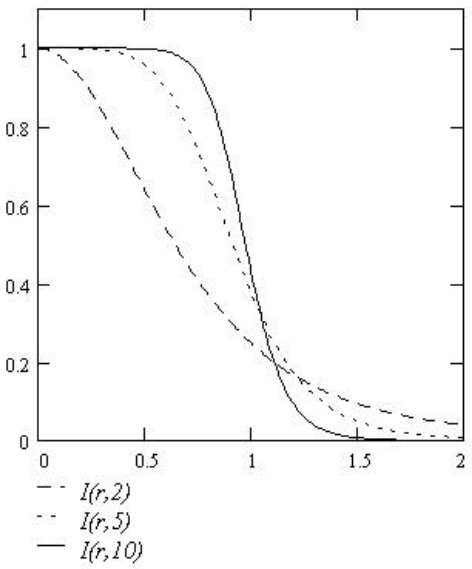

Fig. 1: *soft flat-top distribution according to eq. 2*

References

[1] Y. Li, "Light beams with flat-topped profiles", Opt. Lett. **27**, (2002), p. 1007.

Wave aberrations due to a cover layer, a problem reconsidered

K.-H. Brenner

The observation of object details behind a cover layer of different refractive index plays an important role in many areas of optics. In microscopy, e.g. the cover layer cannot be avoided, when the objects to be observed are suspended in a solution. In disk type optical storage, the cover layer is necessary to protect the information pits from dust and scratches. The aberrations induced by a cover layer are most prominently observable in the case of imaging through a beam splitter cube, if the imaging rays are not parallel. From these examples it apparent, that the amount of aberrations must depend on the cover layer thickness *d* and the aperture angle ϑ, (see fig. 1). A thorough treatment of wave aberrations resulting from imaging through a cover layer was given by Török et al. [1]. According to this theory, the aberration phase is given by:

$$\Phi = -k_0\, d\left(n_1 \cos J_1 - n_2 \cos J_2\right) \qquad (1)$$

where k_0 is the wave number in vacuum, *d* is the cover layer thickness and n_j, J_j are the refractive indices and the aperture angles in the corresponding media. The aperture angles are related by Snell's law. An alternative approach for the aberration phase was given by Braat [2]. It resulted in a phase, which differs significantly from the result in equation 1. This discrepancy has started a discussion on what is the most appropriate way to define or to measure wave aberrations in such a configuration. One aspect of the problem arises particularly, because the rays of a perfect spherical wave will not focus at the same spot. Since eq. 1 also deviated significantly from our experimental results, we have reconsidered the problem of aberrations resulting from a cover layer.

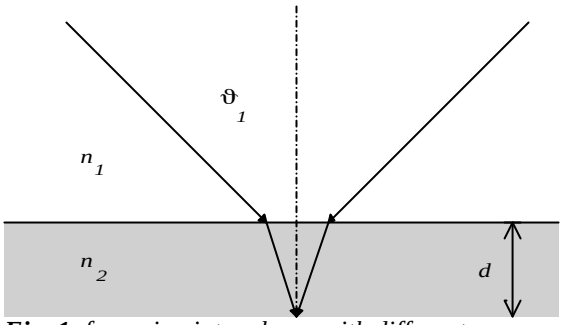

Fig. 1: *focussing into a layer with different refractive index*

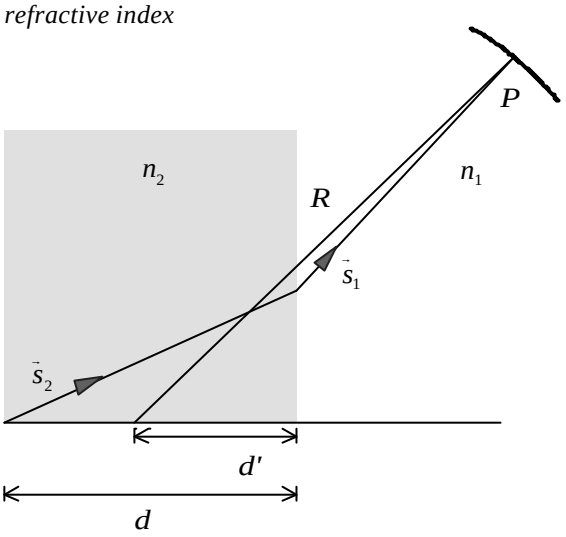

Fig. 2: *geometry for analysing the wave aberations*

Our configuration for describing the wave aberration is depicted in fig. 2. We invert the ray directions and start at the ideal focus in a depth *d*. The ray with direction unit vector $\vec{s}_2$ intersects the surface and is refracted to a new direction vector $\vec{s}_1$. If we extend this vector by an arbitrary length factor a, we reach a point *P* in space. The ideal wave front at *P* originates from the paraxial focus, which is in a depth $d' = d\, n_1 / n_2$. As an intermediate definition for the wave aberration, we define the optical path length difference between the path from the ray origin to point *P* and the ideal wave front radius *R*, derived from the distance of *P* from the paraxial focus. This definition is, of course, dependent on the length factor a. Considering the limiting case, where a approaches infinity, we obtain an alternative form of the wave aberration phase, given by:

$$\Phi = -k_0\left(n_1\, d' \cos J_1 - n_2\, d \cos J_2\right) \quad \text{with } d' = \frac{n_1}{n_2} d \qquad (2)$$

It differs from eq. 1 only in the first term where the thickness is replaced by the effective thickness *d'*. This result appears similar to Braat's result and agrees perfectly with our experimentally observed aberration phase.

References

[1] P. Török, P. Varga, G.R. Booker, " Electromagnetic diffraction of light focused through a planar interface between materials of mismatched refractive indices: structure of the electromagnetic field.", J. Opt. Soc. Am. A, **12**, (1995) p. 2136

[2] J. Braat, "Analytical expression for the aberration coefficients of a tilted plane parallel plate", Appl. Opt. **36**, (1997) p. 8459.

Equivalence of the law of refraction and constant path length for focused systems

K.-H. Brenner

The main ingredients for the geometrical optical design of optical beam shaping elements are the law of power conservation, the law of refraction and the constant optical path-length condition. From Lagrange's invariant, it can be suspected, that the later two are interrelated, since the derivation of this invariant requires the validity of the law of refraction [1]. For a focussed optical system, as depicted in fig. 1, it is possible, to show very quickly that the constant optical path-length condition and the law of refraction are in fact equivalent relations.

We consider an optical path through the system, characterised by the refractive indices n_j and the unit direction vectors $\vec{s}_j$ in the corresponding regions. The points of intersection with the surface are denoted as $\vec{r}_j$.

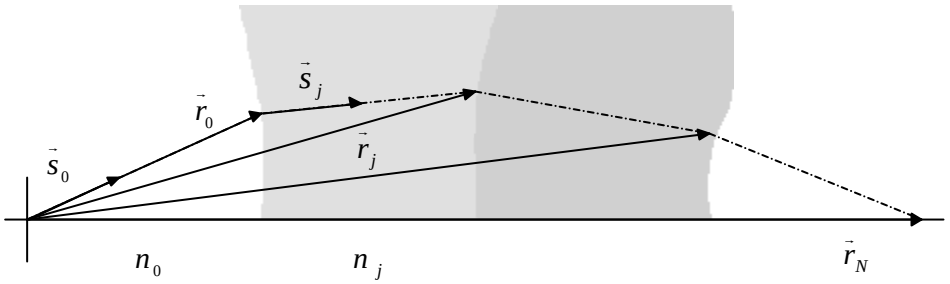

With *N-1* surfaces, the last point $\vec{r}_N$ is the focus, assumed to be fixed and located on the optical axis. The constant optical path-length condition, in this nomenclature, can be described as:

$$OPL = n_0\left|\vec{r}_0\right| + n_1\left|\vec{r}_1 - \vec{r}_0\right| + \ldots + n_j\left|\vec{r}_j - \vec{r}_{j-1}\right| + \ldots + n_{N-1}\left|\vec{r}_{N-1} - \vec{r}_N\right| = const \tag{1}$$

Consequently, a variation of the OPL must be zero: $d\left(OPL\right) = 0$ (2)

By denoting $r = \left|\vec{r}\right|$ and using the vector relation $\vec{r}\ d\vec{r} = r\ dr$, we can write eq. 2 as:

$$\left(n_0 \frac{\vec{r}_0}{\left|\vec{r}_0\right|} - n_1 \frac{\vec{r}_1 - \vec{r}_0}{\left|\vec{r}_1 - \vec{r}_0\right|}\right) d\vec{r}_0 + \ldots + \left(n_j \frac{\vec{r}_j - \vec{r}_{j-1}}{\left|\vec{r}_j - \vec{r}_{j-1}\right|} - n_{j+1} \frac{\vec{r}_{j+1} - \vec{r}_j}{\left|\vec{r}_{j+1} - \vec{r}_j\right|}\right) d\vec{r}_j + \ldots - n_{N-1}\left(\frac{\vec{r}_{N-1} - \vec{r}_N}{\left|\vec{r}_{N-1} - \vec{r}_N\right|}\right) d\vec{r}_N = 0 \tag{3}$$

Note that the last term with a negative sign vanishes, since the last point is fixed, therefore $d\vec{r}_N = 0$. From fig. 1, it is apparent, that

$$\frac{\vec{r}_0}{\left|\vec{r}_0\right|} \equiv \vec{s}_0 \text{ and } \frac{\vec{r}_j - \vec{r}_{j-1}}{\left|\vec{r}_j - \vec{r}_{j-1}\right|} \equiv \vec{s}_j$$

Thus eq. 3 simplifies to

$$\left(n_0\vec{s}_0 - n_1\vec{s}_1\right) d\vec{r}_0 + \ldots + \left(n_j\vec{s}_j - n_{j+1}\vec{s}_{j+1}\right) d\vec{r}_j + \ldots + \left(n_{N-2}\vec{s}_{N-2} - n_{N-1}\vec{s}_{N-1}\right) d\vec{r}_j = 0 \tag{4}$$

Since the variations can be chosen freely, this condition can only be meet if

$$\left(n_j\vec{s}_j - n_{j+1}\vec{s}_{j+1}\right) d\vec{r}_j = 0 \tag{5}$$

Realising that the vector $d\vec{r}_j$ is tangential to surface *j*, eq. 5 is an alternate form of the law of refraction, stating that the surface normal is perpendicular to the surface tangent. This shows that the law of refraction can be derived from the equal path-length condition. By reversing the derivations, the equal path-length condition could likewise be derived from the law of refraction. Thus, for a system designed on the basis of the law of refraction, the equal path-length condition does not add new information.

References

[1] Born and Wolf, "Principles of Optics", 7th Edition, Cambridge University Press 1997, p. 135

List of recent publications

(1) M. Kufner, S. Kufner, S. Voigt, "A refractive free space micro-optical 4x4 interconnect with aspherical lenses and optical fan-out", 274. WE-Heraeus-Seminar on Microoptics, Bad Honnef, 22.-24.04.2002

(2) Ulrich Ehrbächer, Karl-Heinz Brenner, "Theoretical and experimental investigation of collimation properties of microlenses", 274. WE-Heraeus-Seminar on Microoptics, Bad Honnef, 22.-24.04.2002

(3) K.-H. Brenner, "Three dimensional Micro-integration of optical systems", 274. WE-Heraeus-Seminar on Microoptics, Bad Honnef, 22.-24.04.2002

(4) D. Dragoman, M. Dragoman, K.-H. Brenner " Tomographic amplitude and phase recovery of vertical-cavity surface emitting lasers using the ambiguity function", Optics Letters. Vol. **27**, No. 17, 1519 – 1521, ISSN 0146-9592 (2002)

(5) Wolf, Henning, Dr, 72622 Nürtingen; Brenner, Karl-Heinz, Prof. Dr., 68309 Mannheim; Bähr, Jochen, Dr., 69190 Walldorf, " Projektionsverfahren und Projektor", Anmeldetag: 05.10.1994, DE 44 35 599.8, Erteilung – Patent-Nr. 195 02 660, IPC: G02B 27/46 (2002)

(6) Daniela Dragoman, Mircea Dragoman, and Karl-Heinz Brenner, "Amplitude and phase recovery of rotationally symmetric beams", Applied Optics, Vol. **41**, No. 26, 5512 – 5518, ISSN 0003-6935 (2002)

(7) K.-H. Brenner, P. Kümmel, U. Krackhardt: "Wellenoptische Optimierung des Schreib-/Lesekopfes für die hochdichte optische Speicherung", *Simulation in Physik, Informatik und Informationstechnik (SYSI),* 43 – 48, ISSN 0944-7121, 66. Physikertagung, Leipzig (2002)

(8) U. W. Krackhardt, S. Flammuth, "Micro-Integration of optical Modules for Angle Division Multiplexing", *ORT 2002*, Proceedings 7th Workshop Optics in Computing Technology, 19 - 26, ISSN 1437-8507, Mannheim (2002)

(9) X. Liu, K.-H. Brenner, "Reconstruction of two-dimensional complex amplitudes from intensity measurements", *IOG 2002*, Proceedings 1st Workshop Information Optics, 67 – 73, ISSN 1684-7296, Mannheim (2002)

(10) J. Bähr, K.-H. Brenner, "Realisierung abbildender Mikrooptiken durch Ionenaustauschtechniken in Glas", Buchbeitrag in *Handbuch Mikrotechnik*, Herausgeber Wolfgang Ehrfeld, Carl Hanser Verlag München, ISBN 3-446-21506-9, 347 – 406 (2002)

(11) U. Brüning, U. Krackhardt, "Systeme für eine hocheffiziente elektrische und optische Kurzstreckenübertragung im SAN Bereich", *it-Information Technology*, Oldenbourg Wissenschaftsverlag München, **45**. Jahrgang, Heft-Nr. 2, 65 – 71, ISSN 1611-2776 (2003)

(12) X. Liu, K.-H. Brenner, "Reconstruction of two-dimensional complex amplitudes from intensity measurements", Optics Communications **225**, p. 19 - 30, (2003)